Journal of Materials Chemistry C

PAPER

View Article Online
View Journal | View Issue

Cite this: J. Mater. Chem. C, 2019, 7, 8874

Towards boosting the exciton lifetime and efficiency of near-infrared aggregation induced emitters with hybridized local and charge transfer excited states: a multiscale study†

Jianzhong Fan, ‡ Yuchen Zhang,‡ Kai Zhang, Jie Liu, Guanyu Jiang, Feiyan Li, Lili Lin * and Chuan-Kui Wang*

Fluorescent emitters with long exciton lifetime and high luminescence efficiency show promising application in organic light emitting diodes (OLEDs), especially those with an aggregation induced emission (AIE) feature. However, theoretical studies on emitters with amorphous structure with the consideration of the solid-state effect (SSE) are limited. In this work, a multiscale simulation is performed to study the photophysical properties of the reported compound 4,4′-(naphtho[2,3-*c*][1,2,5]thiadiazole-4,9-diyl)bis(*N*,*N*-diphenylaniline) (NZ2TPA) and a theoretically designed promising compound 4,4′-(naphtho-[2,3-c][1,2,5]oxadiazole-4,9-diyl)bis(*N*,*N*-diphenylaniline) (NO2TPA), which both possess unique features of near-infrared (NIR) emission, aggregation induced emission and hybridized local and charge transfer (HLCT) excited states. The packing modes of the two kinds of molecules in film are obtained by molecular dynamics (MD) simulations, and then the photophysical properties with the consideration of the SSE are studied by using the combined quantum mechanics and molecular mechanics (QM/MM) method. Finally, the exciton evolution process is revealed by the rate equations. The results show that geometrical changes between the ground state (S_0) and the first singlet excited state (S_1) are restricted in film. Moreover, we find that the Huang–Rhys (HR) factor and reorganization energy in film are much smaller than those in the gas phase due to the suppressed rotation motion in the low frequency region. Thus, the non-radiative energy consumption process is hindered by the restricted intramolecular rotation effect, which results in larger values of fluorescence efficiency for NZ2TPA (28.5%) and NO2TPA (34.9%) in film compared to those (0.11% and 0.21%) in the gas phase; this indicates the AIE and HLCT mechanisms. Furthermore, our designed NO2TPA compound is demonstrated to be a more efficient AIE–HLCT-NIR molecule with a longer exciton lifetime (600 ns) compared to that of NZ2TPA (25 ns). Thus, a promising molecule NO2TPA with boosted exciton lifetime and efficiency is proposed. Furthermore, this work could enrich the theoretical calculation method to investigate the luminescence properties of organic molecules in OLEDs.

Received 23rd April 2019,
Accepted 1st July 2019

DOI: 10.1039/c9tc02144b

rsc.li/materials-c

1. Introduction

Recently, thermally activated delayed fluorescence (TADF) materials have attracted continuous interest due to their high exciton utilization in organic light emitting diodes (OLEDs).[1–5] TADF materials have been regarded as third generation materials after the first generation conventional fluorescence and the second generation phosphorescence materials. As efficient TADF molecules, the energy gap (ΔE_{ST}) between the first singlet excited state (S_1) and the first triplet excited state (T_1) should be small enough for the up-conversion process of triplet excitons. According to the equation $\Delta E_{ST} = 2\int\int \Phi_L(1)\Phi_H(2)\frac{e^2}{r_1 - r_2}\Phi_L(2)\Phi_H(1)dr_1dr_2$, one efficient way to obtain a small ΔE_{ST} is decreasing the spatial overlap between the highest occupied molecular orbital (HOMO) and lowest unoccupied molecular orbital (LUMO). Thus, a rapid reverse intersystem crossing (RISC) rate from T_1 to S_1 can be obtained, according to the equation $k_{RISC} \approx \exp(-\Delta E_{ST}/k_BT)$, where k_B is the Boltzmann constant and T is the temperature.[6–8] However, following the relationships $f \propto \mu^2$ and $\mu = \int\int \phi_L(1)\phi_H(2)r_{12}\phi_L(2)\phi_H(1)dr_1dr_2$, where f and μ represent the oscillator strength and transition dipole moment respectively, one negative effect is inevitably generated. Namely, a small orbital overlap for S_1 with a charge transfer (CT) feature gives a slow

Shandong Province Key Laboratory of Medical Physics and Image Processing Technology, Institute of Materials and Clean Energy, School of Physics and Electronics, Shandong Normal University, 250014 Jinan, China.
E-mail: ckwang@sdnu.edu.cn, linll@sdnu.edu.cn

† Electronic supplementary information (ESI) available. See DOI: 10.1039/c9tc02144b

‡ These two authors contributed equally to this work.

radiative rate and low luminescence efficiency.[9–12] Thus, the relationship between high exciton utilization and high efficiency needs to be carefully balanced. To solve this problem, Ma's group put forward the design strategy of fluorescence emitters with hybridized local and charge transfer (HLCT) excited states. The HLCT state is an important excited state for the design of efficient OLED materials, because two compatible characteristics, high-efficiency fluorescence radiation from a local excited (LE) state and a weakly bound exciton which is responsible for the full exciton utilization from a CT state, are combined. Thus, both a high photoluminescence efficiency and a large fraction of singlet exciton generation in electroluminescence can be simultaneously achieved in molecules with a HLCT feature.[13–17] Moreover, previous studies show that emitters need to be dispersed into host matrices to suppress the effect of aggregation caused quenching (ACQ) and exciton annihilation. This makes the device fabrication process complicated and gives serious efficiency roll-off at high luminance; all these issues impede the wide application of new generation OLEDs. Fortunately, Tang *et al.* proposed the aggregation induced emission (AIE) concept. AIE is regarded as a promising strategy to solve the abovementioned quenching and annihilation problems, and the application of non-doped OLEDs with AIE features has become a research hotspot in recent years.[18–22] Furthermore, near-infrared (NIR) emitting materials show promising application in bio-imaging, chemo-sensing, full-color displays and so on.[23–26] The development of highly efficient NIR emitting molecules is necessary because NIR molecules typically show relatively low luminescence efficiency due to their large non-radiative decay rate, which increases exponentially with the emission wavelength, governed by the energy gap law. Thus, the development of high efficiency non-doped NIR OLEDs is desired. Tremendous efforts have been made, for example, Su and Yang reported a non-doped device exhibiting excellent NIR emission with a maximum external quantum efficiency of 0.82%.[27] Lu *et al.* reported a strong NIR fluorescent emitter with the external quantum efficiency of a non-doped NIR OLED reaching 2.58%,[28] and so on.[29–31]

Recently, Yang and Ma proposed a D–π–A–π–D type NIR molecule 4,4′-(naphtho[2,3-*c*][1,2,5]thiadiazole-4,9-diyl)bis(*N*,*N*-diphenylaniline) NZ2TPA (shown in Fig. 1(a)), which possesses HLCT and AIE characteristics.[32] The non-doped device based on NZ2TPA shows excellent performance with a maximum external quantum efficiency of 3.9% and exhibits low efficiency roll-off. NZ2TPA is the most efficient emitter in the reported non-doped NIR fluorescent OLEDs. Thus, theoretical investigations to reveal the inner AIE and HLCT mechanisms as well as the exciton evolution process for red or NIR emitters in neat film are necessary to develop highly efficient non-doped OLEDs. Recently, new HLCT emitters with enhanced device efficiency and stability are reported.[33,34] Moreover, Brédas pointed out that much theoretical work remains to be done for new generation emitting molecules; one important issue is the consideration of the solid-state effect.[35] This effect plays a significant role in defining the nature of the excited states, and their energies and dynamics. Thus, explicit consideration of intermolecular interactions in the solid phase is required. This goal can be achieved by hybrid methods involving quantum mechanics and molecular mechanics (QM/MM) calculations combined with molecular dynamics (MD) simulations.

In this article, a multiscale simulation is performed to study the photophysical properties and reveal the fundamental factors that lead to enhanced emission of NZ2TPA in neat film. The brief process is described below. Firstly, the film structure of NZ2TPA is obtained by MD simulations. Secondly, the molecular properties in film are studied by using the QM/MM method, which takes the surrounding molecular effects into consideration. Thirdly, the excited-state dynamics and exciton evolution process are investigated by MOMAP and home-built rate equations respectively. Thus, the AIE and HLCT features as well as the exciton evolution process are illustrated and experimental measurements are reasonably explained. Furthermore, a NIR AIE–HLCT molecule 4,4′-(naphtho[2,3-*c*][1,2,5]oxadiazole-4,9-diyl)bis(*N*,*N*-diphenylaniline) NO2TPA (shown in Fig. 1(b)) with the sulfur atom in NZ2TPA replaced by an oxygen atom is designed and studied theoretically. Higher quantum efficiency is found for the NO2TPA molecule than NZ2TPA. Our study will help one better understand the AIE and HLCT properties and also promote the design of new type NIR molecules with boosted exciton lifetime and efficiency.

2. Methodology

2.1 Theoretical method

For emitting molecules with a HLCT feature, the fluorescence efficiency (Φ_F) can be expressed as $\Phi_F = \frac{k_r}{k_r + k_{nr} + k_{ISC}}$, where k_r and k_{nr} represent the radiative and non-radiative decay rate from S_1 to the ground state (S_0) respectively, and k_{ISC} is the intersystem crossing rate between the singlet and triplet states. In order to quantitatively obtain the efficiency, these abovementioned rate parameters need to be calculated firstly.

As for the radiative decay rate k_r, it is calculated by the Einstein spontaneous emission equation, which is written as

$$k_r = \frac{f\Delta E_{fi}^2}{1.499}. \quad (1)$$

Here, f is the oscillator strength and ΔE_{fi} is the vertical emission energy with the unit of wavenumbers (cm^{-1}).[36]

As for the non-radiative decay rate k_{nr}, it can be expressed as the following form according to Fermi's golden rule (FGR) and first-order perturbation theory

$$k_{nr} = \frac{2\pi}{\hbar}\sum_{kl} R_{kl} Z_i^{-1} \times \sum_{vu} e^{-\beta E_{iv}} \left\langle \Theta_{fu} \middle| \hat{P}_{fk} \middle| \Theta_{iv} \right\rangle \left\langle \Theta_{iv} \middle| \hat{P}_{fl} \middle| \Theta_{fu} \right\rangle \delta(E_{iv} - E_{fu}). \quad (2)$$

Here, $R_{kl} = \left\langle \Phi_f \middle| \hat{P}_{fk} \middle| \Phi_i \right\rangle \left\langle \Phi_i \middle| \hat{P}_{fl} \middle| \Phi_f \right\rangle$ is the non-adiabatic electronic coupling and Z_i is the partition function. Φ and Θ are the electronic state and nuclear vibrational wave function respectively. u and v are vibrational quantum numbers, and f and i represent

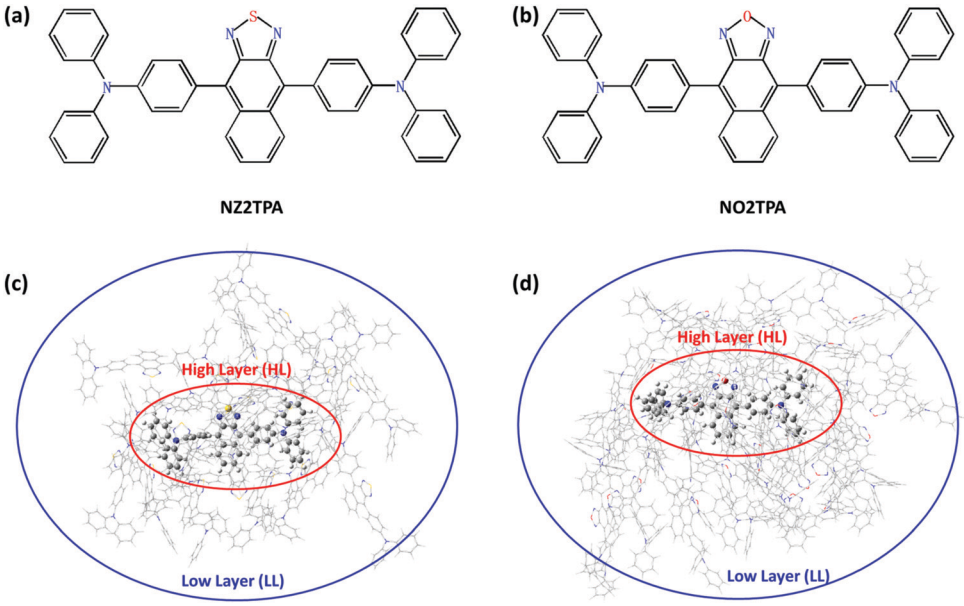

Fig. 1 Chemical structures of NZ2TPA (a) and NO2TPA (b). ONIOM models for NZ2TPA (c) and NO2TPA (d): surrounding molecules are regarded as the low layer and the centered molecule is treated as the high layer.

the final and initial state respectively. Furthermore, applying the Fourier transform of the delta function and the Franck–Condon principle, eqn (2) can be written as

$$k_{nr} = \sum_{kl} \frac{1}{\hbar^2} R_{kl} \int_{-\infty}^{\infty} dt \left[e^{i\omega_{if} t} Z_i^{-1} \rho_{ic,kl}(t, T) \right]. \quad (3)$$

where $\rho_{ic,kl}(t,T)$ is the thermal vibration correlation function (TVCF), which is written as $\rho_{ic,kl}(t,T) = \mathrm{Tr}\left(\widehat{P}_{fk} e^{-i\tau_f \widehat{H}_f} \widehat{P}_{fl} e^{-i\tau_i \widehat{H}_i}\right) = \int_{-\infty}^{\infty} dx' \left\langle x' \middle| \widehat{P}_{fk} e^{-i\tau_f \widehat{H}_f} \widehat{P}_{fl} e^{-i\tau_i \widehat{H}_i} \middle| x' \right\rangle$. Here, the vector x' represents the excited-electronic state normal mode coordinates and $\widehat{P}_{fk} = -i\hbar \frac{\partial}{\partial Q_{fk}}$ represents the normal momentum operator of the kth normal mode in the final electronic state. All these parameters can be calculated by MOMAP (Molecular Materials Property Prediction Package). Details of the methodology and application can be found in Peng's and Shuai's work.[37–40] Besides, the vibration-mode mixing effect can be taken into accounts as $Q_{ik} = \sum_{l}^{3n-6} S_{kl} Q_{fl} + D_k$. Here, S is the Duschinsky rotation matrix representing the mixing of normal modes in the initial and final states and the vector D_k is the displacement along normal mode k. All these parameters and reorganization energies can be projected onto the internal coordinates by Reimers' algorithm.[41]

As for the intersystem crossing rate k_{ISC}, it is calculated by the Marcus rate equation, which is written as

$$k_{ISC} = \frac{H_{SO}^2}{\hbar} \sqrt{\frac{\pi}{k_B T \lambda}} \exp\left[-\frac{(\lambda + \Delta E)^2}{4\lambda k_B T} \right]. \quad (4)$$

Here H_{SO} is the spin–orbit coupling (SOC) coefficient and it can be calculated by the Dalton 2013 package.[42] λ is the Marcus reorganization energy and k_B denotes the Boltzmann constant. T represents the temperature, which is set as 298 K here. ΔE is the adiabatic energy gap between the final state and the initial state. For example, when we want to calculate the ISC rate from S_1 to T_1, ΔE is expressed as $\Delta E = E_T - E_S$ where E_T and E_S are the energy of T_1 and S_1 respectively. In addition, if we need calculate the RISC rate from T_1 to S_1, ΔE is written as $\Delta E = E_S - E_T$.[43–45]

Moreover, in this work, the internal conversion (IC) rate k_{IC} from a highly excited state to a low excited state, such as the second singlet excited state (S_2) to S_1, is roughly estimated by the equation

$$\log(k_{IC}/s^{-1}) \approx 12 - 2\Delta\nu/\mu m^{-1}. \quad (5)$$

Here, $\Delta\nu = \Delta E/hc$ and ΔE is the energy gap between the relevant states.[46]

Furthermore, based on the abovementioned rate parameters, the exciton evolution process of NZ2TPA and NO2TPA is described by the following four-energy-level and five-energy-level rate equations respectively.

Details of the four-energy-level rate equation for NZ2TPA are as follows

$$\frac{d\rho_{S_0}}{dt} = \rho_{S_1} k_r + \rho_{S_1} k_{nr}. \quad (6)$$

$$\frac{d\rho_{S_1}}{dt} = -\rho_{S_1} k_r - \rho_{S_1} k_{nr} + \rho_{S_2} k_{S_2 \to S_1} + \rho_{T_2} k_{T_2 \to S_1}. \quad (7)$$

$$\frac{d\rho_{S_2}}{dt} = -\rho_{S_2} k_{S_2 \to S_1} - \rho_{S_2} k_{S_2 \to T_2} + \rho_{T_2} k_{T_2 \to S_2}. \quad (8)$$

$$\frac{d\rho_{T_2}}{dt} = -\rho_{T_2} k_{T_2 \to S_1} - \rho_{T_2} k_{T_2 \to S_2} + \rho_{S_2} k_{S_2 \to T_2}. \quad (9)$$

Details of the five-energy-level rate equation for NO2TPA are as follows

$$\frac{d\rho_{S_0}}{dt} = \rho_{S_1}k_r + \rho_{S_1}k_{nr}. \quad (10)$$

$$\frac{d\rho_{S_1}}{dt} = -\rho_{S_1}k_r - \rho_{S_1}k_{nr} + \rho_{S_2}k_{S_2\to S_1} + \rho_{T_2}k_{T_2\to S_1}. \quad (11)$$

$$\frac{d\rho_{S_2}}{dt} = -\rho_{S_2}k_{S_2\to S_1} - \rho_{S_2}k_{S_2\to T_2} - \rho_{S_2}k_{S_2\to T_5} + \rho_{T_5}k_{T_5\to S_2}. \quad (12)$$

$$\frac{d\rho_{T_2}}{dt} = -\rho_{T_2}k_{T_2\to S_1} + \rho_{S_2}k_{S_2\to T_2} + \rho_{T_5}k_{T_5\to T_2}. \quad (13)$$

$$\frac{d\rho_{T_5}}{dt} = -\rho_{T_5}k_{T_5\to T_2} - \rho_{T_5}k_{T_5\to S_2} + \rho_{S_2}k_{S_2\to T_5}. \quad (14)$$

In the above equations, ρS_0, ρS_1, ρS_2, ρT_2 and ρT_5 represent the population number of S_0, S_1, S_2, T_2 and T_5 respectively. Thus, the singlet and triplet exciton evolution processes are investigated. Detailed illustrations are shown in the following section.

2.2 Computational details

2.2.1 MD simulations. All the all-atom molecular dynamics simulations are carried out using the Gromacs-2016.1 package based on the general AMBER force field (GAFF), which is a well-established force field for organic molecules.[47,48] Moreover, partial charges for NZ2TPA and NO2TPA are obtained by the restrained electrostatic potential (RESP) fitting method.[49] A spherical cut-off of 1.2 nm for the summation of VDW and real space electrostatic interactions and the particle-mesh Ewald (PME) solver for long range electrostatic interactions are used. The film structures of the two studied molecules are simulated by the following procedure: (1) randomly inserting molecules in a 10 × 10 × 10 nm^3 box to generate an initial packing model; (2) compression for an initial 5 ns at 600 K and 100 bar to make the molecules close together; (3) another 10 ns simulation at 600 K and 1 bar, then cooling from 600 K down to 298 K gradually within 3 ns; and (4) equilibration simulation for 20 ns at 298 K and 1 bar. Here, some issues need to be clarified – the velocity rescaling (V-rescale) thermostat and Berendsen barostat are applied for the temperature and pressure control processes,[50,51] while for the final 10 ns in the equilibration simulation process, the Noseé–Hoover thermostat and the Parrinello–Rahman barostat are used to obtain equilibrium configurations.[52–54] Finally, the representative film structures of NZ2TPA and NO2TPA are acquired by cluster analysis; the corresponding results are shown in Fig. S1 and S2 (ESI†).

2.2.2 QM/MM calculations. After getting the structures of the two systems by MD simulations, the molecular photophysical properties in film are investigated by QM/MM calculations with the two-layer ONIOM approach in the Gaussian 16 package;[55] the corresponding models for NZ2TPA and NO2TPA are shown in Fig. 1(c) and (d). In this model, the central single molecule is regarded as the high layer and calculated by the QM method with cam-B3LYP and the 6-31G(d) basis set, while the surrounding molecules are regarded as the low layer and treated by the MM method. Moreover, electronic embedding is adopted and the surrounding molecules are frozen in our QM/MM calculations.[56–58]

Furthermore, based on these basic molecular data, the normal mode analyses for the Huang–Rhys (HR) factor and reorganization energy are performed using the DUSHIN program,[59] and the SOC coefficient is calculated using the Dalton 2013 package.[42] Then, the non-radiative decay rate and (R)ISC rate are calculated by MOMAP and the Marcus equation respectively. Finally, the exciton evolution processes of NZ2TPA and NO2TPA are investigated using the four-energy-level and five-energy-level rate equations respectively.

3. Results and discussion

3.1 Molecular geometries

Since the photophysical properties of light-emitting molecules are closely related to their molecular structures, thus, we firstly study the geometrical structures of NZ2TPA and NO2TPA for the S_0 and S_1 states in the gas phase and film respectively. Some dihedral angles and bond lengths are marked in Fig. S1(a and b) (ESI†), and the corresponding data are collected in Table 1. For NZ2TPA in the gas phase, the calculated $\theta1$ and $\theta5$, $\theta2$ and

Table 1 Geometry parameters of S_0 and S_1 for NZ2TPA and NO2TPA in the gas phase and film. θ and B represent the dihedral angle and bond length respectively, which are marked in Fig. S1 (ESI). Δ represents the variation between the gas phase and film

	NZ2TPA						NO2TPA					
	Gas			Film			Gas			Film		
	S_0	S_1	Δ	S_0	S_1	Δ	S_0	S_1	Δ	S_0	S_1	i
$\theta1$	111.1	112.0	0.9	69.6	70.7	1.1	111.8	114.1	2.3	84.8	83.0	1.8
$\theta2$	68.4	65.7	2.7	75.9	75.7	0.2	68.6	66.6	2.0	66.6	69.1	2.5
$\theta3$	121.9	135.1	13.2	94.4	91.1	3.3	129.4	147.0	17.6	126.5	133.8	7.3
$\theta4$	122.7	135.6	12.9	128.3	139.4	11.1	126.7	139.5	12.8	136.7	143.9	7.2
$\theta5$	111.4	114.2	2.8	65.7	59.4	6.3	114.0	116.2	2.2	66.2	60.0	6.2
$\theta6$	67.4	64.9	2.5	79.6	73.4	6.2	68.2	66.4	1.8	93.1	96.1	3.0
$B1$	1.413	1.402	0.111	1.409	1.408	0.001	1.411	1.400	0.011	1.412	1.408	0.004
$B2$	1.483	1.459	0.025	1.480	1.476	0.004	1.481	1.454	0.027	1.481	1.462	0.019
$B3$	1.483	1.458	0.025	1.477	1.447	0.030	1.480	1.543	0.063	1.473	1.448	0.025
$B4$	1.413	1.401	0.012	1.410	1.393	0.017	1.410	1.399	0.011	1.413	1.402	0.011

$\theta 6$ as well as $\theta 3$ and $\theta 4$ are almost the same in the S_0 state with a largest variation of 1.0° (68.4°–67.4° = 1.0°), and a similar condition can be found for the S_1 state. Thus, the molecular structure of NZ2TPA is almost symmetrical in the gas phase, either for the S_0 or S_1 state. Remarkable changes between S_0 and S_1 for the NZ2TPA molecule in the gas phase can be found with a value of 13.2°, 12.9° and 0.111 Å for $\theta 3$, $\theta 4$ and $B1$ respectively. Moreover, these changes are decreased to 3.3°, 11.1° and 0.001 Å in film. Thus, restricted geometry changes are found when the molecule is in film. Similar variations can be found for NO2TPA in that the changes of $\theta 3$ and $\theta 4$ between S_0 and S_1 become smaller from 17.6° and 12.8° in the gas phase to 7.3° and 7.2° in film respectively. Thus, the surrounding molecules' effect on the geometric structures is highlighted.

In order to quantitatively characterize this effect, the root mean squared displacement (RMSD) with the expression $\mathrm{RMSD} = \sqrt{\frac{1}{N}\sum_{i}^{\mathrm{natom}}\left[(x_i - x_i')^2 + (y_i - y_i')^2 + (z_i - z_i')^2\right]}$ is analyzed and the value of the RMSD between S_0 and S_1 is calculated using Multiwfn.[60] The corresponding data are shown in Fig. 2. The results show that the geometric changes of NZ2TPA between S_0 and S_1 in the gas phase are more significant than that in film with a RMSD value of 0.613 Å and 0.127 Å respectively. For NO2TPA, the RSMD value between S_0 and S_1 is 0.626 Å in the gas phase and it decreases to 0.096 Å in film. All these results indicate that the geometry variations are restricted by the environment. Furthermore, to confirm our deduction, the dihedral angle is scanned with a step of 5° and the rotation angle is defined as the dihedral angle after rotation minus the dihedral angle at equilibrium. The corresponding data for NZ2TPA and NO2TPA are shown in Fig. 3 and Fig. S3 (ESI†). We know that the rotational energy barrier (kcal mol^{-1}), which is defined as the energy difference between the configuration after rotation and S_0, is much higher for the molecule in film than that in the gas phase. The results confirm that the rotation for the molecule in film is much more difficult than that in the gas phase.

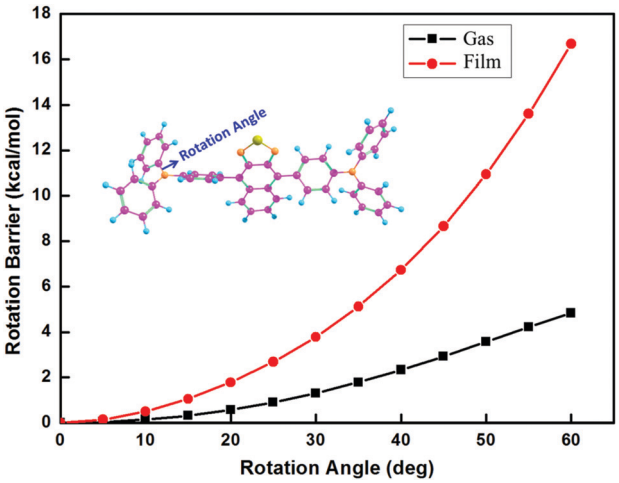

Fig. 3 Rotational energy barriers (kcal mol^{-1}) for NZ2TPA in the gas phase (black line) and film (red line) respectively.

All these differences can influence the transition property, Huang–Rhys factor and reorganization energy. Moreover, the non-radiative energy consumption path of the excited state could be hindered and enhanced fluorescence efficiency can be expected for the molecule in film. The different geometric change involved in the transition in the gas phase and in film is shown to have a close relationship with the photophysical properties in a later section.

3.2 Energy scheme and transition properties

In order to illustrate the exciton evolution process, the energy scheme should be analyzed firstly. The calculated adiabatic

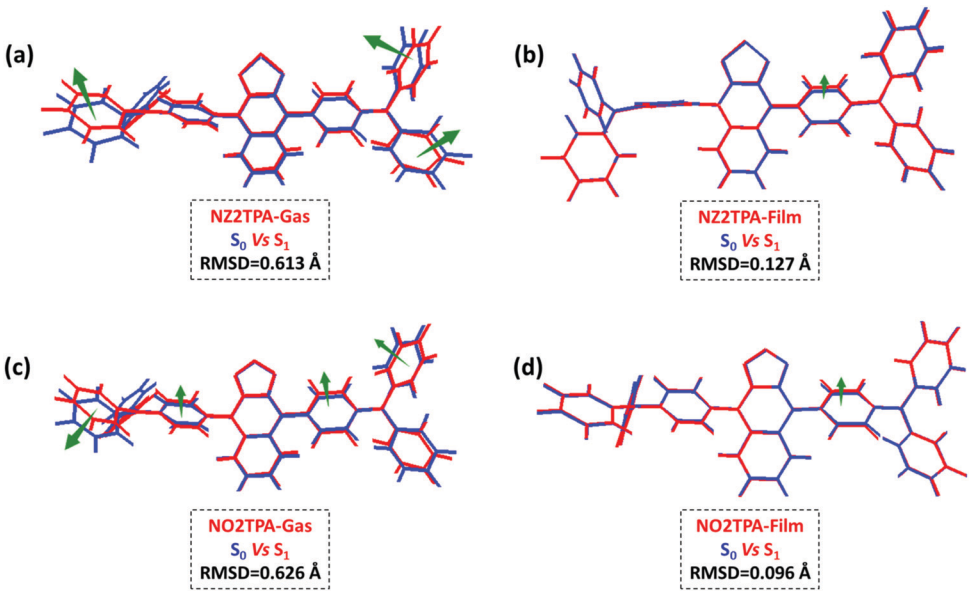

Fig. 2 Geometry changes between S_0 and S_1 in the gas phase and film for NZ2TPA (a and b) and NO2TPA (c and d) respectively.

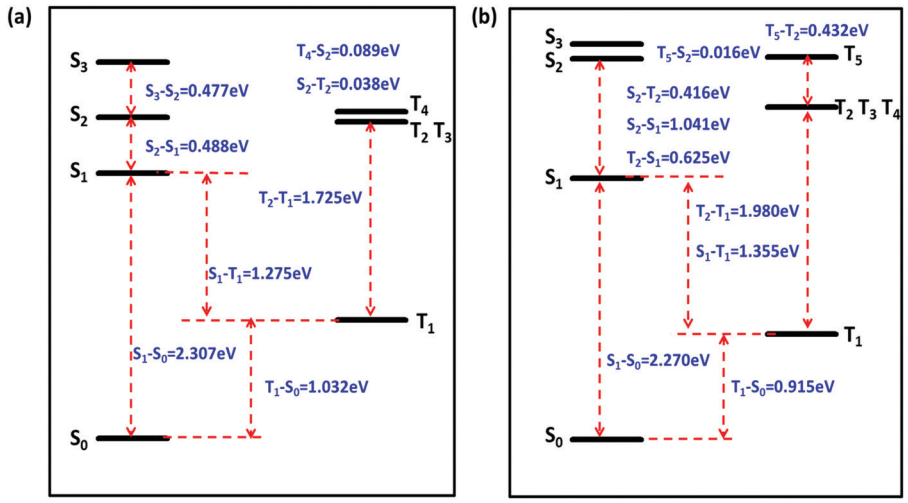

Fig. 4 Adiabatic excitation energies for NZ2TPA (a) and NO2TPA (b) in film respectively.

excitation energy landscapes for NZ2TPA and NO2TPA in film and in the gas phase are shown in Fig. 4 and Fig. S4 (ESI†) respectively. The results show that the S_1–T_1 gap is 1.275 eV for NZ2TPA, which indicates that the measured exciton utilization (33%), which is larger than the theoretical threshold for singlet excitons (25%), is not derived from TADF, and the phosphorescence emission is not observed in neat film at 77 K. Moreover, no additional energy level is found between S_1 and T_1; the spin–vibronic mechanism proposed by Penfold and Marian can be neglected, which proved to be an important factor for ISC and RISC processes of TADF molecules.[61–64] Thus, we can exclude the routes of phosphorescence and TADF for NZ2TPA. Furthermore, the calculated T_2–T_1 gap (1.725 eV) is large enough to block the internal conversion process of triplet excitons from T_2 to T_1, while the calculated T_4–S_2 gap (0.089 eV) and S_2–T_3 (T_2) gap (0.038 eV) as well as the T_2–S_1 gap (0.450 eV) are small enough to promote the ISC and RISC processes, and the spin–vibronic effect between these states may accelerate the conversion process. All these results correspond well with the proposed HLCT mechanism by Ma, and a ''hot exciton'' transition from a high triplet state to a singlet state could occur for NZ2TPA. As for NO2TPA, the S_1–T_1 gap (1.355 eV) and T_2–T_1 gap (1.980 eV) are large, the RISC process from T_1 to S_1 and the internal conversion process from T_2 to T_1 can be excluded, and ''hot exciton'' conversion can also be expected. Moreover, the calculated T_2, T_3 and T_4 are degenerate; the conversion process from a high triplet state to a singlet state may be different from that of NZ2TPA. More evidence is provided in a later section.

Furthermore, the excited state properties are related to their transition properties. Thus, the highest occupied natural transition orbital (HONTO) and the lowest unoccupied natural transition orbital (LUNTO) are calculated, and natural transition orbital (NTO) analyses of the involved states in the energy landscape are also performed for NZ2TPA and NO2TPA in film, with the corresponding results shown in Fig. 5 and 6. In order to illustrate the effect of the molecular surroundings, NTO analyses are also performed for the two molecules in the gas phase; the results are shown in Fig. S5 and S6 (ESI†). In addition, the excited-state wave functions are further exploited to quantitatively evaluate their LE and CT contributions; the results are collected in Table 2 and Table S1 (ESI†). We know that the S_1 state exhibits dominant LE characteristics with a ratio of 77% and 80% for NZ2TPA and NO2TPA in film respectively, and the predominant LE feature could give remarkable fluorescence emission compared with TADF molecules whose S_1 possesses a CT feature. Moreover, for NZ2TPA in film, S_2 and T_2 are dominated by CT with a ratio of 82% and 75% respectively. As for T_3 and T_4, they possess substantial LE character (55% and 76%), which indicates a large overlap between the corresponding transition orbitals. As for NO2TPA, a significant LE character (80%) is also observed for the S_1 state, and S_2 is classified as CT with a ratio of 59%. As for the triplet states, they all exhibit a LE feature with a ratio of 66%, 53%, 80% and 70% for T_2, T_3, T_4 and T_5 respectively. Thus, different transition characteristics can be found for singlet and triplet states. In addition, non-adiabatic coupling between ^{3}LE and ^{3}CT promotes the ISC and RISC processes through the second-order coupling effect.[65,66] Detailed studies on this issue for HLCT molecules will be performed in the future.

3.3 Huang–Rhys factor and reorganization energy

In this section, the Huang–Rhys (HR) factor and reorganization energy are analyzed to illustrate the non-radiative energy consumption and the AIE mechanism. As for the HR factor, it is calculated by the equation $\mathrm{HR}_k = \frac{w_k D_k^2}{2\hbar}$, where ω_k is the vibration frequency and D_k is the normal coordinate displacement of mode k. The calculated HR factors *versus* the normal mode frequencies for NZ2TPA and NO2TPA in the gas phase and film are shown in Fig. 7(a, b) and 8(a, b) respectively. For NZ2TPA in the gas phase, the large values of the HR factor are all in the low frequency region (<200 cm^{-1}), such as 15.66 (8.54 cm^{-1}), 2.07 (45.62 cm^{-1}) and 1.26 (84.12 cm^{-1}), which correspond to the rotation motion of benzene as shown in the

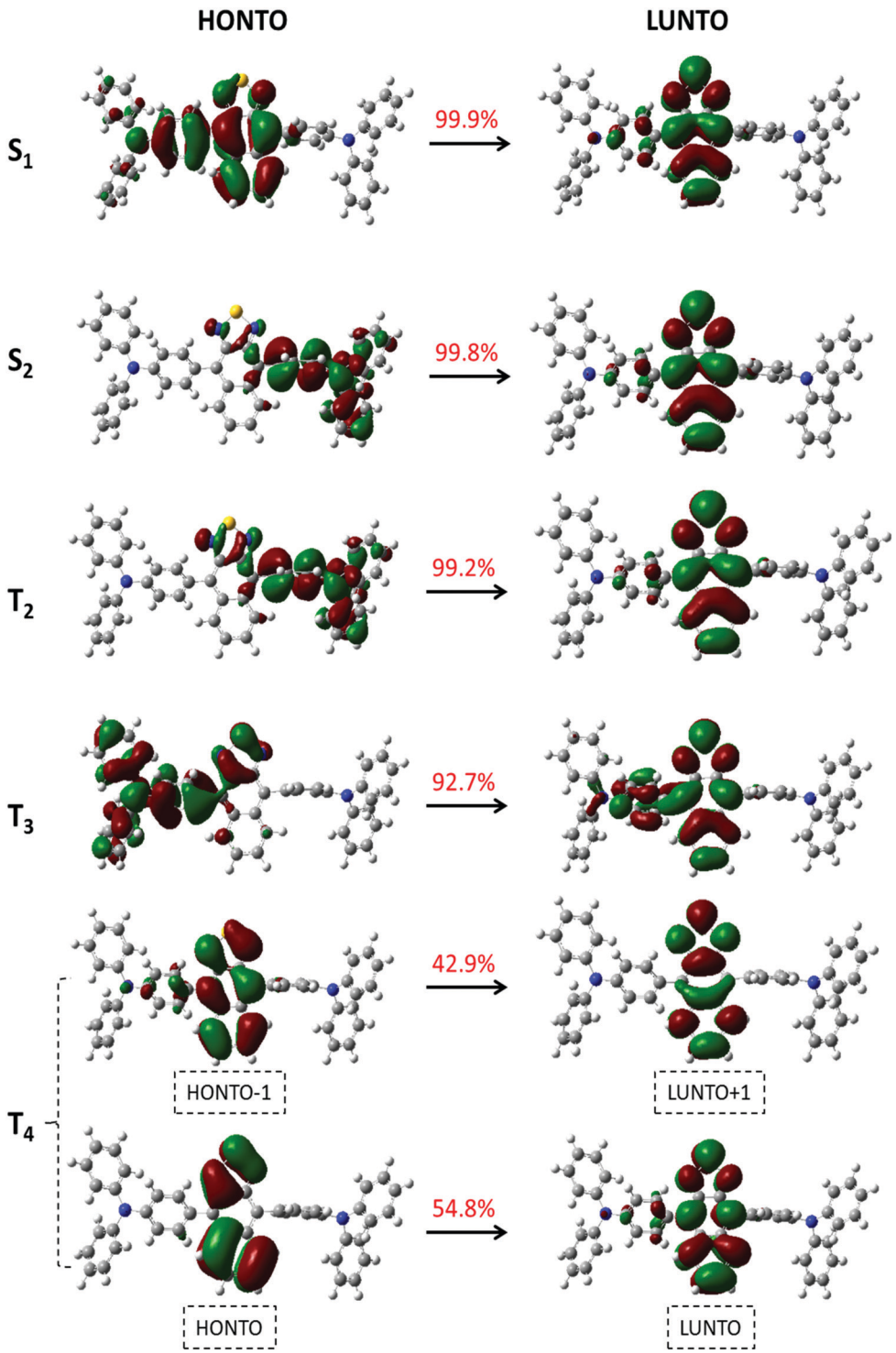

Fig. 5 Transition characteristics for selected singlet and triplet excited states for NZ2TPA in film (isovalue = 0.02).

insets. Moreover, all HR factors are decreased for NZ2TPA in film with HR factors of 0.68 (40.18 cm^{-1}) and 0.90 (97.38 cm^{-1}). These results correspond well with the abovementioned geometry analysis in Section 3.1 in which the RMSD is decreased from 0.613 Å in the gas phase to 0.127 Å in film. As for NO2TPA, a similar situation can be found. The large values of the HR factor are also distributed in the low frequency region (<200 cm^{-1}), for example 3.94 (9.64 cm^{-1}), 18.20 (10.79 cm^{-1}), 2.54 (17.52 cm^{-1}) and 2.13 (46.10 cm^{-1}). These values are all decreased in film with the largest one being 0.72 (157.58 cm^{-1}). The corresponding RMSD value is 0.626 Å in the gas phase and it decreases to 0.096 Å in film. Thus, geometry variations are restricted by the intermolecular interaction and the effect of the surrounding molecules is highlighted.

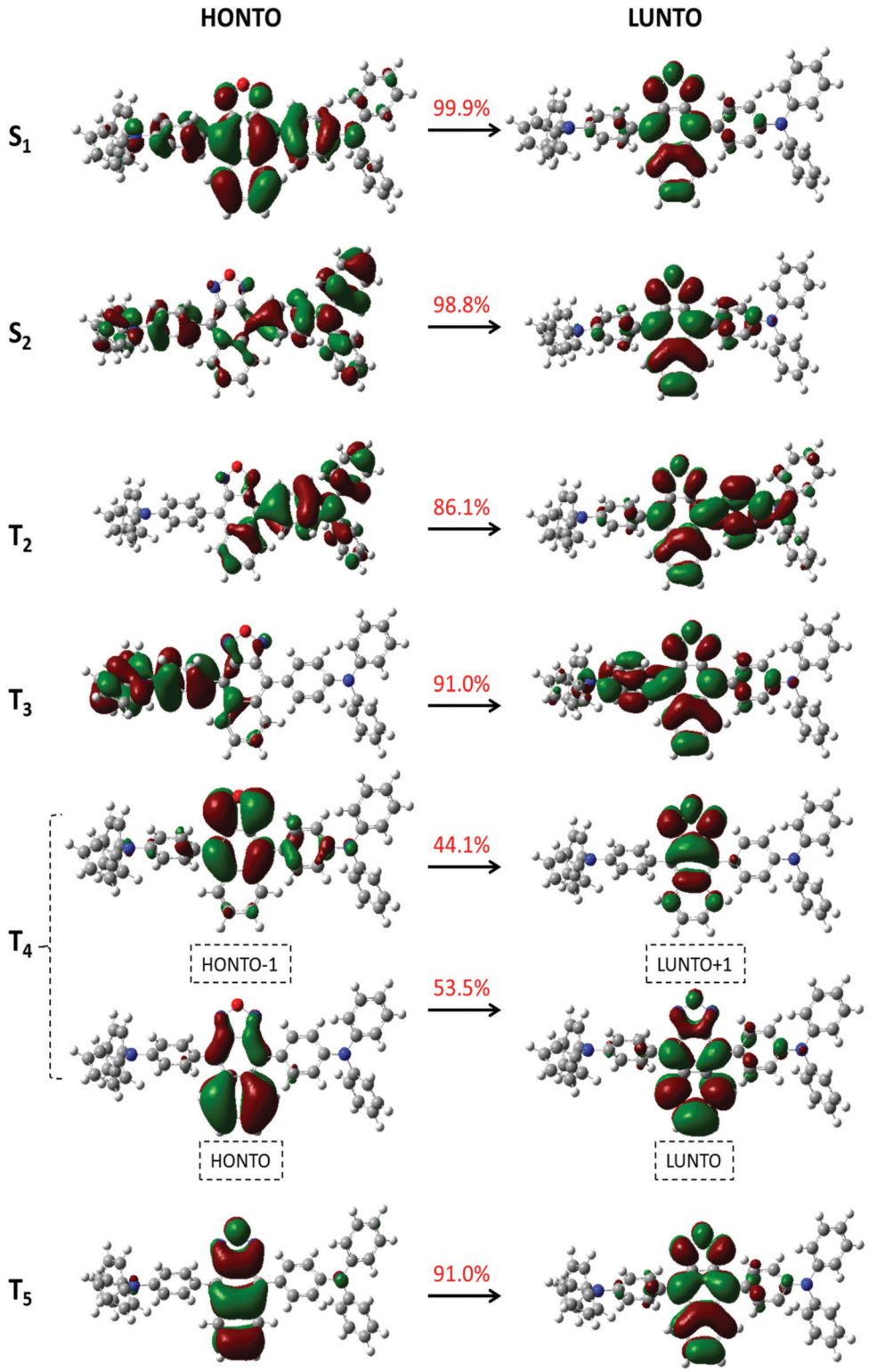

Fig. 6 Transition characteristics for selected singlet and triplet excited states for NO2TPA in film (isovalue = 0.02).

As for the reorganization energy, it can be obtained by the equation $\lambda = \sum_k \hbar w_k \mathrm{HR}_k$; the calculated reorganization energies *versus* the normal mode frequencies for NZ2TPA and NO2TPA in the gas phase and film are shown in Fig. 7(c, d) and 8(c, d) respectively. The results show that the reorganization energy of NZ2TPA in the gas phase is 81.6 meV in the low frequency region (<200 cm^{-1}) and 244.4 meV in the high frequency region (>200 cm^{-1}) respectively. While for the molecule in film, it correspondingly changes to 39.6 meV in

Table 2 Calculated charge transfer (CT) and local excitation (LE) character (in %) for selected singlet and triplet excited states of NZ2TPA and NO2TPA in film

	NZ2TPA		NO2TPA	
	LE (%)	CT (%)	LE (%)	CT (%)
S_1	77	23	80	20
S_2	18	82	41	59
T_2	25	75	66	34
T_3	55	45	53	47
T_4	76	24	80	20
T_5	—	—	70	30

the low frequency region and 246.2 meV in the high frequency region. The total decrease in reorganization energy from the gas phase (326.0 meV) to film (285.8 meV) is 40.2 meV, which is mainly contributed by the reduction in the low frequency region (42.0 meV). As for NO2TPA in the gas phase, the reorganization energy is 93.1 meV and 239.0 meV in the low and high frequency regions respectively, and they accordingly become 34.3 meV and 240.1 meV in film. The total reorganization energy decreases from 332.1 meV in the gas phase to 274.4 meV in film. The reduced reorganization energy (57.7 meV) still mainly comes from the reduction in the low frequency region (58.8 meV). Thus, the reorganization energy in the low frequency region is decreased in a rigid environment for both molecules.

In order to investigate the relationship between the photophysical properties and the molecular structures, the reorganization energy is projected onto the internal coordinates. Contributions from the bond length, bond angle and dihedral angle are collected in Table 3 and the corresponding proportions are shown in Fig. S7 (ESI†). For NZ2TPA, the contribution from the bond length takes the major part either in the gas phase (60.5%) or in film (67.8%). Moreover, the contribution from the dihedral angle is significantly decreased from 28.9% (94.2 meV) in the gas phase to 14.8% (42.2 meV) in film. Further, the total decrease in reorganization energy from the gas phase to film is 40.2 meV and it is mainly contributed by the reduction of the dihedral angle (52.0 meV). As for NO2TPA, the contribution from the bond length also accounts for the majority (58.6% in the gas phase and 72.5% in film), and the decreased reorganization energy from gas to film (57.7 meV) is also mainly contributed by the decrement of the dihedral angle (68.2 meV). All these data correspond well with the analysis of the molecular geometries in Section 3.1. Thus, the non-radiative energy consumption process of S_1 is measured by the Huang–Rhys factor and reorganization energy. The results confirm that the rotation motion in the low frequency region can be suppressed in film, non-radiative energy consumption of the excited state is suppressed and enhanced fluorescent efficiency could be expected in film. Hence, the effect of the surrounding molecules is highlighted and the AIE mechanism is revealed. In addition to restricted intramolecular motions, there are several mechanisms for AIE, such as inaccessibility of the conical intersection, non-Kasha processes and the impact of supramolecular organization and interactions.[67–70] However, in this work, we think the non-radiative energy consumption process is hindered by the restricted intramolecular rotation effect. More precise illustrations are being pursued.

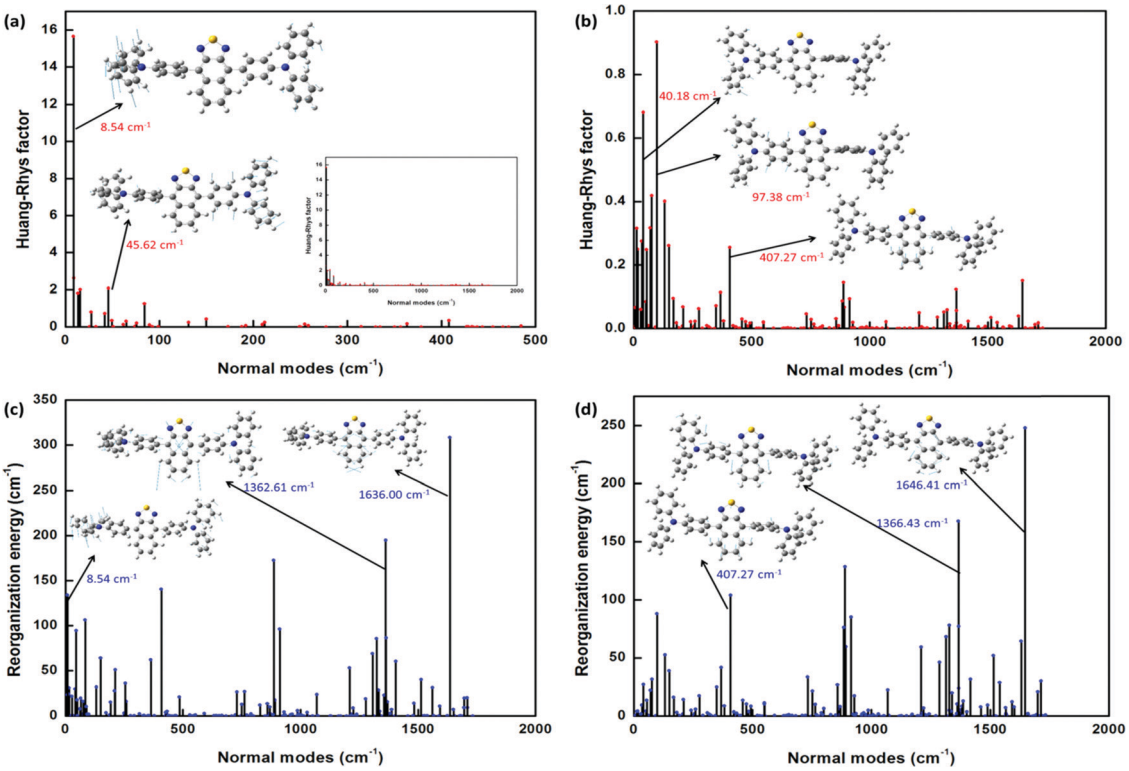

Fig. 7 Calculated HR factors *versus* normal mode frequencies in the gas phase (a) and film (b) as well as the reorganization energies *versus* normal mode frequencies in the gas phase (c) and film (d) for NZ2TPA. Representative vibration modes are shown as insets.

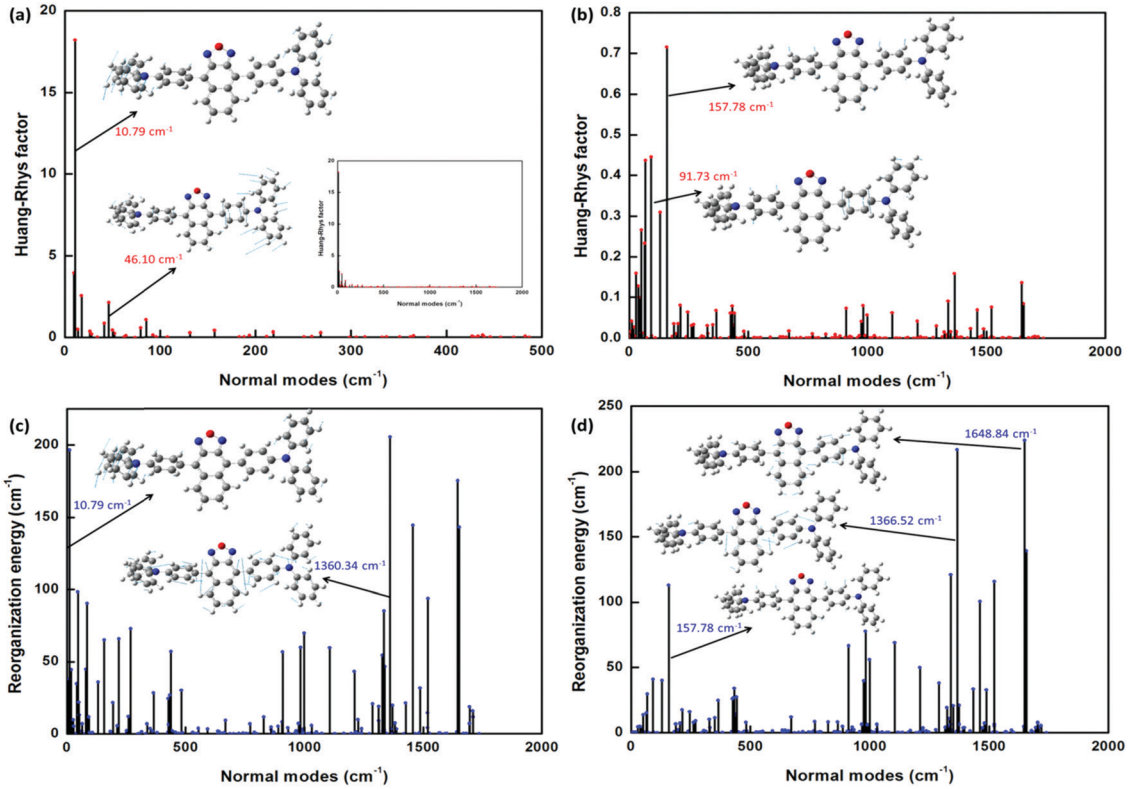

Fig. 8 Calculated HR factors *versus* normal mode frequencies in the gas phase (a) and film (b) as well as the reorganization energies *versus* normal mode frequencies in the gas phase (c) and film (d) for NO2TPA. Representative vibration modes are shown as insets.

Table 3 Reorganization energies (meV) from the bond length, bond angle and dihedral angle in the gas phase and film are listed respectively. $\Delta_{Gas-Film}$ represents the energy difference between the gas phase and film

	NZ2TPA			NO2TPA		
	Gas	Film	$\Delta_{Gas-Film}$	Gas	Film	$\Delta_{Gas-Film}$
Bond length	197.3	193.9	3.4	194.5	198.9	−4.4
Bond angle	34.5	49.7	−15.2	27.6	33.7	−6.1
Dihedral angle	94.2	42.2	52.0	110.0	41.8	68.2
Total	326.0	285.8	40.2	332.1	274.4	57.7

Table 4 Calculated emission wavelength, oscillator strength (*f*) and electric transition diploe moment (EDM) are listed. k_r and k_{nr} represent the radiative and non-radiative decay rate from S_1 to S_0 respectively

		Wavelength (nm)	*f*	EDM (D)	k_r (s^{-1})	k_{nr} (s^{-1})
NZ2TPA	Gas	648.1	0.4916	8.23	7.81×10^7	7.28×10^{10}
	Film	613.3	0.3590	6.85	6.37×10^7	1.60×10^8
NO2TPA	Gas	645.1	0.6636	9.54	1.06×10^8	4.99×10^{10}
	Film	625.9	0.4979	8.14	8.48×10^7	1.58×10^8

3.4 Excited-state dynamics and exciton evolution process

In the abovementioned sections, the non-radiative decay process and HLCT as well as the AIE mechanism are qualitatively studied by analyzing the geometry changes, RMSD, energy landscape, HR factor and reorganization energy. Here, radiative and non-radiative rate parameters are quantitatively calculated and the excited-state dynamics is investigated. Furthermore, the exciton evolution process is illustrated. Firstly, the radiative and non-radiative decay rates from S_1 to S_0 are calculated by the method illustrated in the "Theoretical method" section, and the corresponding data are collected in Table 4. The results indicate that the calculated fluorescence wavelength in film is blue-shifted compared with that in the gas phase; this is caused by intermolecular interactions in a rigid environment. Moreover, the emission wavelength of NO2TPA (625.9 nm) is red-shifted compared with that of NZ2TPA (613.3 nm); this could be caused by the stronger electronegativity of oxygen than sulfur as well as their different packing modes in film. From the experimental measurement that NZ2TPA is a near-infrared molecule in non-doped OLEDs, the designed NO2TPA is expected to be a highly efficient NIR molecule. Furthermore, the calculated radiative decay rate of NZ2TPA is smaller in film (6.37×10^7 s^{-1}) than that in the gas phase (7.81×10^7 s^{-1}); this is due to the smaller oscillator strength (0.3590) and transition dipole moment (6.85 D) in film. The non-radiative decay rate is largely decreased in film (1.60×10^7 s^{-1}) compared with that in the gas phase (7.28×10^{10} s^{-1}). All results highlight the effect of the surrounding molecules and verify the AIE mechanism. As for NO2TPA, the radiative rate is also decreased from 1.06×10^8 s^{-1} in the gas phase to 8.48×10^7 s^{-1} in film, and this is related to the smaller oscillator strength (0.4979) and transition dipole moment (8.14 D) in film. Moreover, the non-radiative

decay rate is also decreased from 4.99×10^{10} s^{-1} in the gas phase to 1.58×10^{8} s^{-1} in film; the non-radiative energy consumption path of the excited state is hindered. In order to verify the accuracy of the calculated K_{nr}, the log K_{nr} (ΔE) parabola is shown in Fig. S8 (ESI†); no vibrational feature is found in the gas phase and film. Furthermore, the calculated SOC constant, reorganization energy and non-adiabatic energy gap between S_1 and T_1 are 0.092 cm^{-1}, 102.5 meV and 1275 meV respectively for NZ2TPA in film; the ISC rate is estimated to be zero. Similarly, the SOC constant, reorganization energy and S_1–T_1 gap are 0.647 cm^{-1}, 107.7 meV and 1355 meV respectively for NO2TPA in film; the calculated ISC is zero. Thus, the ISC process from S_1 to T_1 for HLCT molecules NZ2TPA and NO2TPA can be neglected. So, based on the equation $\phi_F = \frac{k_r}{k_r + k_{nr} + k_{ISC}}$, the calculated fluorescence efficiency of NO2TPA (34.9%) is higher than that of NZ2TPA (28.5%). Thus, as NZ2TPA is the most efficient NIR fluorescent molecule in the reported non-doped OLEDs, a more efficient NIR molecule NO2TPA with HLCT and AIE features is theoretically proposed.

In order to study the excited-state dynamics and exciton evolution process of NZ2TPA and NO2TPA in film, the ISC and RISC rates between selected singlet and triplet states are calculated and the corresponding data are collected in Tables 5 and 6. For NZ2TPA, the calculated SOC constants between S_2 and T_3 are 2.665 cm^{-1} and 2.777 cm^{-1}; the ISC (7.87×10^{9} s^{-1}) and RISC (1.95×10^{9} s^{-1}) between them are larger than the others. Moreover, the triplet excitons translate to singlet excitons through the channels $T_3 \rightarrow S_1$ and $T_2 \rightarrow S_1$ with a rate of 1.39×10^{8} s^{-1} and 1.53×10^{7} s^{-1} respectively. As for NO2TPA, the ISC and RISC rates between T_5 and S_2 are 3.70×10^{6} s^{-1} and 9.46×10^{7} s^{-1}; this is caused by the larger SOC constant based on T_5 (1.278 cm^{-1}) than that based on S_2 (0.185 cm^{-1}). Moreover, the calculated ISC rates from S_2 to T_2, T_3 and T_4 are 8.42×10^{7} s^{-1}, 4.81×10^{7} s^{-1} and 5.09×10^{7} s^{-1} respectively, while for the RISC rates from T_2, T_3 and T_4 to S_2, they are small and the RISC processes can be neglected. Fortunately, triplet excitons can also be efficiently utilized through the ISC channels from T_2, T_3 and T_4 to S_1 with a rate of 1.06×10^{7} s^{-1}, 3.97×10^{6} s^{-1} and 1.80×10^{6} s^{-1} respectively. Thus, the "hot exciton" mechanism is revealed for NZ2TPA and NO2TPA.

Based on the abovementioned rate parameters and the calculated energy landscapes (shown in Fig. 4), the exciton evolution processes of NZ2TPA and NO2TPA in film are described by the four-energy-level and five-energy-level rate equations respectively. The corresponding results are shown in Fig. 9, and the time enlargement sections are shown in Fig. S9 and S10 (ESI†). As for NZ2TPA, the internal conversion rate from S_2 to S_1 is roughly estimated to be 1.63×10^{11} s^{-1}. Moreover, as T_2 and T_3 are degenerate, the ISC and RISC rates between S_2 and T_2 are calculated by the equations $k_{ISC} = \frac{k_{S_2 \rightarrow T_2}{}^2 + k_{S_2 \rightarrow T_3}{}^2}{k_{S_2 \rightarrow T_2} + k_{S_2 \rightarrow T_3}}$ and $k_{RISC} = \frac{k_{T_2 \rightarrow S_2}{}^2 + k_{T_3 \rightarrow S_2}{}^2}{k_{T_2 \rightarrow S_2} + k_{T_3 \rightarrow S_2}}$. Thus, the ISC and RISC between S_2 and T_2 are 7.56×10^{9} s^{-1} and 1.86×10^{9} s^{-1} respectively. Similarly, the calculated ISC from T_2 to S_1 is 1.28×10^{8} s^{-1}. As Fig. 9(c) and Fig. S9 (ESI†) show, the initial population numbers of S_2 (ρ_{S_2}) and T_2 (ρ_{T_2}) are assumed as 0.25 and 0.75 respectively, and then the singlet exciton is rapidly transformed from S_2 to S_1. After 0.004 ns, the population number of S_1 exceeds that of S_2. Moreover, the triplet exciton in T_2 is also quickly converted to S_1, and they keep the same value at 0.23 ns. Meanwhile, the occupancy of S_1 reaches the maximum number at 1.12 ns. At the same time, the singlet exciton in S_1 converts to S_0 through radiative and non-radiative decay processes, and the population number of S_0 (ρ_{S_0}) is dominant after 3.53 ns. Finally, excited state excitons are depleted at about 25 ns; the exciton evolution processes are finished. As for NO2TPA, representative rate parameters and exciton evolution processes are shown in Fig. 9(b), (d) and Fig. S10 (ESI†). In 0–0.1 ns, the population numbers of S_1 and especially T_2 rapidly increase, which is due to the large internal conversion rates from high energy levels. After 3.03 ns, the population number of S_0 exceeds that of S_1. Then, ρ_{S_0} is further increased with the reduction of ρ_{T_2} and they reach the same value at 53.0 ns. Finally, the excited state exciton processes are finished at about 600 ns. Thus, through investigating the excited-state dynamics and exciton evolution process, a more efficient AIE–HLCT-NIR molecule NO2TPA with longer exciton lifetime is proposed, compared with NZ2TPA.

Table 5 Calculated intersystem crossing (ISC) and reverse intersystem crossing (RISC) rates between selected singlet and triplet excited states for NZ2TPA in film. SOC and ΔE represent the spin–orbit coupling constant and adiabatic energy difference between two states. k is the rate parameter

	SOC (cm^{-1})	ΔE (meV)	k (s^{-1})
$S_2 \rightarrow T_3$	2.665	−38	7.87×10^{9}
$S_2 \rightarrow T_2$	0.673	−38	3.40×10^{8}
$T_3 \rightarrow S_2$	2.777	38	1.95×10^{9}
$T_2 \rightarrow S_2$	0.759	38	9.74×10^{7}
$T_3 \rightarrow S_1$	0.631	−450	1.39×10^{8}
$T_2 \rightarrow S_1$	0.219	−450	1.53×10^{7}

Table 6 Calculated ISC and RISC rates between selected singlet and triplet excited states for NO2TPA in film

	SOC (cm^{-1})	ΔE (meV)	k (s^{-1})
$T_5 \rightarrow S_2$	0.185	−16	3.70×10^{6}
$S_2 \rightarrow T_5$	1.278	16	9.46×10^{7}
$S_2 \rightarrow T_4$	0.365	−415	5.09×10^{7}
$S_2 \rightarrow T_3$	0.353	−416	4.81×10^{7}
$S_2 \rightarrow T_2$	0.527	−416	8.42×10^{7}
$T_4 \rightarrow S_2$	0.384	415	5.64×10^{0}
$T_3 \rightarrow S_2$	0.573	416	1.10×10^{1}
$T_2 \rightarrow S_2$	0.449	416	5.42×10^{0}
$T_4 \rightarrow S_1$	0.222	−626	1.80×10^{6}
$T_3 \rightarrow S_1$	0.345	−625	3.97×10^{6}
$T_2 \rightarrow S_1$	0.735	−625	1.06×10^{7}

4. Conclusion

The solid-state effect on the excited-state dynamics of NZ2TPA and NO2TPA in film is theoretically investigated by a

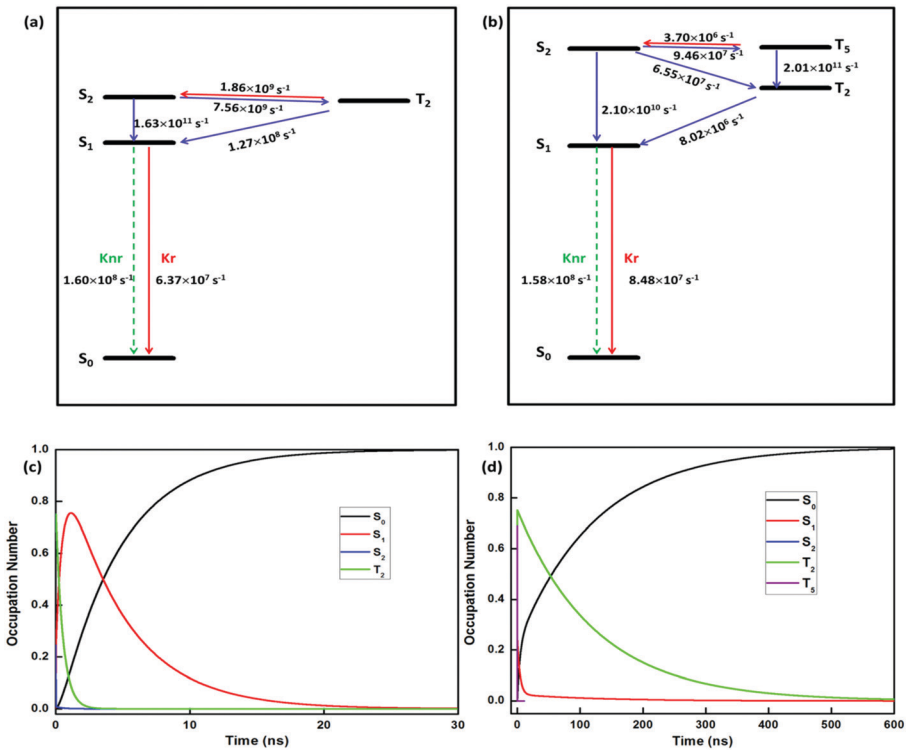

Fig. 9 Four-level model for NZ2TPA (a) and five-level model for NO2TPA (b). Exciton evolution process for NZ2TPA (c) and NO2TPA (d).

multiscale simulation. The film structures are obtained by MD simulations and the solid-state effect is taken into consideration by the QM/MM method. Finally, the excited state properties of the molecules of interest are studied and the exciton evolution process is revealed. Through the investigation, one knows that the geometry changes between S_0 and S_1 are restricted in film, and the torsion barriers are increased. In addition, the rotation motions in the low frequency region are effectively suppressed by the rigid environment in film, which makes the HR factors and reorganization energies all decrease. Thus, non-radiative energy consumption of the excited state is hindered and enhanced fluorescence efficiencies are found for NZ2TPA and NO2TPA (28.5% and 34.9%) in film compared with those (0.11% and 0.21%) in the gas phase. Moreover, by combing the energy landscapes with the calculated ISC and RISC rates, the excited-state dynamics of the two molecules are analyzed and the ''hot exciton'' channels are revealed. The calculated exciton lifetimes of NZ2TPA and NO2TPA are about 25 ns and 600 ns respectively. Thus, compared with the reported NZ2TPA, a more efficient AIE–HLCT-NIR molecule NO2TPA with boosted exciton lifetime and efficiency is theoretically proposed. This work not only explores the solid-state effect on the excited state properties, but also promotes the development of a theoretical method for practical device environments.

Conflicts of interest

There are no conflicts of interest to declare.

Acknowledgements

This work is supported by the National Natural Science Foundation of China (Grant No. 11874242 and 11374195) and Shandong Provincial Natural Science Foundation, China (ZR2019MA056). Thanks is given for the support of Taishan Scholar Project of Shandong Province and the Scientific Research Foundation of Shandong Normal University. Thanks is given for the support of the Project funded by China Postdoctoral Science Foundation (Grant No. 2018M642689). Great thanks is given to Professor Yi Luo, Professor Zhigang Shuai and Qian Peng for their helpful suggestions in our calculations. Thanks is given to Professor Yingli Niu for his great help in the usage of MOMAP.

References

1 H. Uoyama, K. Goushi, K. Shizu, H. Nomura and C. Adachi, *Nature*, 2012, **492**, 234.
2 T. Huang, W. Jiang and L. Duan, *J. Mater. Chem. C*, 2018, **6**, 5577–5596.
3 Y. Zou, S. Gong, G. Xie and C. Yang, *Adv. Opt. Mater.*, 2018, **6**, 1800568.
4 M. Y. Wong and E. Zysman-Colman, *Adv. Mater.*, 2017, **29**, 1605444.
5 Y. Tao, K. Yuan, T. Chen, P. Xu, H. Li, R. Chen, C. Zheng, L. Zhang and W. Huang, *Adv. Mater.*, 2014, **26**, 7931–7958.
6 Q. Zhang, B. Li, S. Huang, H. Nomura, H. Tanaka and C. Adachi, *Nat. Photonics*, 2014, **8**, 326.

7 L. Gan, K. Gao, X. Cai, D. Chen and S.-J. Su, *J. Phys. Chem. Lett.*, 2018, **9**, 4725–4731.
8 K. J. Kim, G. H. Kim, R. Lampande, D. H. Ahn, J. B. Im, J. S. Moon, J. K. Lee, J. Y. Lee, J. Y. Lee and J. H. Kwon, *J. Mater. Chem. C*, 2018, **6**, 1343–1348.
9 T. Liu, L. Zhu, C. Zhong, G. Xie, S. Gong, J. Fang, D. Ma and C. Yang, *Adv. Funct. Mater.*, 2017, **27**, 1606384.
10 J.-X. Chen, W. Liu, C.-J. Zheng, K. Wang, K. Liang, Y.-Z. Shi, X.-M. Ou and X.-H. Zhang, *ACS Appl. Mater. Interfaces*, 2017, **9**, 8848.
11 J. Fan, Y. Zhang, K. Zhang, L. Lin and C.-K. Wang, *J. Lumin.*, 2019, **209**, 372–378.
12 S. Wu, M. Aonuma, Q. Zhang, S. Huang, T. Nakagawa, K. Kuwabara and C. Adachi, *J. Mater. Chem. C*, 2014, **2**, 421.
13 L. Chen, S. Zhang, H. Li, R. Chen, L. Jin, K. Yuan, H. Li, P. Lu, B. Yang and W. Huang, *J. Phys. Chem. Lett.*, 2018, **9**, 5240–5245.
14 J. Yang, Q. Guo, J. Wang, Z. Ren, J. Chen, Q. Peng, D. Ma and Z. Li, *Adv. Opt. Mater.*, 2018, **6**, 1800342.
15 W. Li, Y. Pan, L. Yao, H. Liu, S. Zhang, C. Wang, F. Shen, P. Lu, B. Yang and Y. Ma, *Adv. Opt. Mater.*, 2014, **2**, 892–901.
16 J. Zhao, B. Liu, Z. Wang, Q. Tong, X. Du, C. Zheng, H. Lin, S. Tao and X. Zhang, *ACS Appl. Mater. Interfaces*, 2018, **10**, 9629–9637.
17 H. Zhang, J. Zeng, W. Luo, H. Wu, C. Zeng, K. Zhang, W. Feng, Z. Wang, Z. Zhao and B. Z. Tang, *J. Mater. Chem. C*, 2019, **7**, 6359–6368.
18 J. Guo, Z. Zhao and B. Z. Tang, *Adv. Opt. Mater.*, 2018, **6**, 1800264.
19 J. Guo, X.-L. Li, H. Nie, W. Luo, R. Hu, A. Qin, Z. Zhao, S.-J. Su and B. Z. Tang, *Chem. Mater.*, 2017, **29**, 3623–3631.
20 J. Huang, H. Nie, J. Zeng, Z. Zhuang, S. Gan, Y. Cai, J. Guo, S.-J. Su, Z. Zhao and B. Z. Tang, *Angew. Chem., Int. Ed.*, 2017, **129**, 13151–13156.
21 F. Ni, Z. Zhu, X. Tong, M. Xie, Q. Zhao, C. Zhong, Y. Zou and C. Yang, *Chem. Sci.*, 2018, **9**, 6150–6155.
22 H. Liu, J. Zeng, J. Guo, H. Nie, Z. Zhao and B. Z. Tang, *Angew. Chem., Int. Ed.*, 2018, **57**, 9290–9294.
23 D.-H. Kim, A. D'Aléo, X.-K. Chen, A. D. S. Sandanayaka, D. Yao, L. Zhao, T. Komino, E. Zaborova, G. Canard, Y. Tsuchiya, E. Choi, J. W. Wu, F. Fages, J.-L. Brédas, J.-C. Ribierre and C. Adachi, *Nat. Photonics*, 2018, **12**, 98–104.
24 J. Xue, Q. Liang, Y. Zhang, R. Zhang, L. Duan and J. Qiao, *Adv. Funct. Mater.*, 2017, **27**, 1703283.
25 H. F. Higginbotham, P. Pander, R. Rybakiewicz, M. K. Etherington, S. Maniam, M. Zagorska, A. Pron, A. P. Monkman and P. Data, *J. Mater. Chem. C*, 2018, **6**, 8219–8225.
26 H. Ye, D. H. Kim, X. Chen, A. S. D. Sandanayaka, J. U. Kim, E. Zaborova, G. Canard, Y. Tsuchiya, E. Y. Choi, J. W. Wu, F. Fages, J.-L. Bredas, A. D'Aléo, J.-C. Ribierre and C. Adachi, *Chem. Mater.*, 2018, **30**, 6702–6710.
27 C. Wang, X.-L. Li, Y. Gao, L. Wang, S. Zhang, L. Zhao, P. Lu, B. Yang, S.-J. Su and Y. Ma, *Adv. Opt. Mater.*, 2017, **5**, 1700441.
28 X. Han, Q. Bai, L. Yao, H. Liu, Y. Gao, J. Li, L. Liu, Y. Liu, X. Li, P. Lu and B. Yang, *Adv. Funct. Mater.*, 2015, **25**, 7521–7529.
29 Q. Zhao and J. Z. Sun, *J. Mater. Chem. C*, 2016, **4**, 10588–10609.
30 H. F. Higginbotham, P. Pander, R. Rybakiewicz, M. K. Etherington, S. Maniam, M. Zagorska, A. Pron, A. P. Monkman and P. Data, *J. Mater. Chem. C*, 2018, **6**, 8219–8225.
31 G. Fu, Y. He, B. Li, L. Liu, W. Li, Z. Zhang and X. Lü, *J. Mater. Chem. C*, 2018, **6**, 8950–8957.
32 T. Liu, L. Zhu, C. Zhong, G. Xie, S. Gong, J. Fang, D. Ma and C. Yang, *Adv. Funct. Mater.*, 2017, **27**, 1606384.
33 C. Fu, S. Luo, Z. Li, X. Ai, Z. Pang, C. Li, K. Chen, L. Zhou, F. Li, Y. Huang and Z. Lu, *Chem. Commun.*, 2019, **55**, 6317–6320.
34 H. Zhang, J. Zeng, W. Luo, H. Wu, C. Zeng, K. Zhang, W. Feng, Z. Wang, Z. Zhao and B. Z. Tang, *J. Mater. Chem. C*, 2019, **7**, 6359–6368.
35 X.-K. Chen, D. Kim and J.-L. Brédas, *Acc. Chem. Res.*, 2018, **51**, 2215–2224.
36 K. Schmidt, S. Brovelli, V. Coropceanu, D. Beljonne, J. Cornil, C. Bazzini, T. Caronna, R. Tubino, F. Meinardi, Z. Shuai and J.-L. Brédas, *J. Phys. Chem. A*, 2007, **111**, 10490–10499.
37 Y. Niu, W. Li, Q. Peng, H. Geng, Y. Yi, L. Wang, G. Nan, D. Wang and Z. Shuai, *Mol. Phys.*, 2018, **116**, 1078–1090.
38 Q. Peng, Y. Yi, Z. Shuai and J. Shao, *J. Am. Chem. Soc.*, 2007, **129**, 9333–9339.
39 Y. Niu, Q. Peng and Z. Shuai, *Sci. China, Ser. B: Chem.*, 2008, **51**, 1153–1158.
40 Z. Shuai and Q. Peng, *Natl. Sci. Rev.*, 2017, **4**, 224–239.
41 J. R. Reimers, *J. Chem. Phys.*, 2001, **115**, 9103–9109.
42 Dalton, a molecular electronic structure program, Release Dalton, 2013, see http://daltonprogram.org.
43 R. Chen, Y. Tang, Y. Wan, T. Chen, C. Zheng, Y. Qi, Y. Cheng and W. Huang, *Sci. Rep.*, 2017, **7**, 6225.
44 L. Lin, Z. Wang, J. Fan and C. Wang, *Org. Electron.*, 2017, **41**, 17–25.
45 P. K. Samanta, D. Kim, V. Coropceanu and J. L. Bredas, *J. Am. Chem. Soc.*, 2017, **139**, 4042–4051.
46 P. Klan and J. Wirz, *Photochemistry of Organic Compounds*, John Wiley&Sons, Chichester, 2009.
47 J. Wang, R. M. Wolf, J. W. Caldwell, P. A. Kollman and D. A. Case, *J. Comput. Chem.*, 2004, **25**, 1157–1174.
48 B. Hess, C. Kutzner, D. van der Spoel and E. Lindahl, *J. Chem. Theory Comput.*, 2008, **4**, 435–447.
49 C. I. Bayly, P. Cieplak, W. Cornell and P. A. Kollman, *J. Phys. Chem.*, 1993, **97**, 10269–10280.
50 G. Bussi, D. Donadio and M. Parrinello, *J. Chem. Phys.*, 2007, **126**, 014101.
51 H. J. C. Berendsen, J. P. M. Postma, W. F. van Gunsteren, A. DiNola and J. R. Haak, *J. Chem. Phys.*, 1984, **81**, 3684–3690.
52 S. Nosé, *J. Chem. Phys.*, 1984, **81**, 511–519.
53 W. G. Hoover, *Phys. Rev. A: At., Mol., Opt. Phys.*, 1985, **31**, 1695–1697.
54 M. Parrinello and A. Rahman, *J. Appl. Phys.*, 1981, **52**, 7182–7190.
55 M. J. Frisch, G. W. Trucks, H. B. Schlegel, G. E. Scuseria, M. A. Robb, J. R. Cheeseman, G. Scalmani, V. Barone,

G. A. Petersson, H. Nakatsuji, X. Li, M. Caricato, A. V. Marenich, J. Bloino, B. G. Janesko, R. Gomperts, B. Mennucci, H. P. Hratchian, J. V. Ortiz, A. F. Izmaylov, J. L. Sonnenberg, F. Ding Williams, F. Lipparini, F. Egidi, J. Goings, B. Peng, A. Petrone, T. Henderson, D. Ranasinghe, V. G. Zakrzewski, J. Gao, N. Rega, G. Zheng, W. Liang, M. Hada, M. Ehara, K. Toyota, R. Fukuda, J. Hasegawa, M. Ishida, T. Nakajima, Y. Honda, O. Kitao, H. Nakai, T. Vreven, K. Throssell, J. A. Montgomery Jr., J. E. Peralta, F. Ogliaro, M. J. Bearpark, J. J. Heyd, E. N. Brothers, K. N. Kudin, V. N. Staroverov, T. A. Keith, R. Kobayashi, J. Normand, K. Raghavachari, A. P. Rendell, J. C. Burant, S. S. Iyengar, J. Tomasi, M. Cossi, J. M. Millam, M. Klene, C. Adamo, R. Cammi, J. W. Ochterski, R. L. Martin, K. Morokuma, O. Farkas, J. B. Foresman and D. J. Fox, *Gaussian 16, revision A.03*, Gaussian Inc., Wallingford CT, 2016.

56 J. Fan, Y. Zhang, Y. Zhou, L. Lin and C.-K. Wang, *J. Phys. Chem. C*, 2018, **122**, 2358–2366.

57 J. Fan, Y. Zhang, K. Zhang, J. Liu, G. Jiang, L. Lin and C.-K. Wang, *Org. Electron.*, 2019, **71**, 113–122.

58 J. Fan, L. Lin and C.-K. Wang, *J. Mater. Chem. C*, 2017, **5**, 8390–8399.

59 J. R. Reimers, *J. Chem. Phys.*, 2001, **115**, 9103–9109.

60 T. Lu and F. W. Chen, *J. Comput. Chem.*, 2012, **33**, 580.

61 J. Gibson, A. P. Monkman and T. J. Penfold, *ChemPhysChem*, 2016, **17**, 2956.

62 J. Gibson and T. Penfold, *Phys. Chem. Chem. Phys.*, 2017, **19**, 8428.

63 T. J. Penfold, F. B. Dias and A. P. Monkman, *Chem. Commun.*, 2018, **54**, 3926–3935.

64 T. J. Penfold, E. Gindensperger, C. Daniel and C. M. Marian, *Chem. Rev.*, 2018, **118**, 6975–7025.

65 W. Zhao, T. S. Cheung, N. Jiang, W. Huang, J. W. Y. Lam, X. Zhang, Z. He and B. Z. Tang, *Nat. Commun.*, 2019, **10**, 1595.

66 R. Huang, J. Avó, T. Northey, E. Chaning-Pearce, P. L. dos Santos, J. S. Ward, P. Data, M. K. Etherington, M. A. Fox, T. J. Penfold, M. N. Berberan-Santos, J. C. Lima, M. R. Bryce and F. B. Dias, *J. Mater. Chem. C*, 2017, **5**, 6269–6280.

67 Q. Li and L. Blancafort, *Chem. Commun.*, 2013, **49**, 5966–5968.

68 X.-L. Peng, S. Ruiz-Barragan, Z.-S. Li, Q.-S. Li and L. Blancafort, *J. Mater. Chem. C*, 2016, **4**, 2802–2810.

69 A. P. Demchenko, V. I. Tomin and P.-T. Chou, *Chem. Rev.*, 2017, **117**, 13353–13381.

70 P. Srujana, P. Sudhakar and T. P. Radhakrishnan, *J. Mater. Chem. C*, 2018, **6**, 9314–9329.